

Electron-cyclotron maser emission from white-dwarf pairs and white-dwarf planetary systems

Andrew J. Willes^{1*} and Kinwah Wu^{2†}

¹*School of Physics, University of Sydney, NSW 2006, Australia*

²*Mullard Space Science Laboratory, University College London, Holmbury St Mary, Dorking, Surrey RH5 6NT*

ABSTRACT

By analogy to Jovian radio emissions powered by the electromagnetic interaction between Jupiter and its moons, we propose that close magnetic-nonmagnetic white-dwarf pairs and white-dwarf planetary systems are strong radio sources. A simple model is developed to predict the flux densities of radio emission generated by a loss-cone-driven electron-cyclotron maser. The radio emission from these systems has high brightness temperatures, is highly polarized, and varies on a periodic cycle following the orbital rotation. Masers from magnetic-nonmagnetic white-dwarf pairs, with orbital periods $\lesssim 10$ min, are expected to be detectable over a wide range of radio frequencies. Terrestrial planets in close orbits about magnetic white dwarfs, with orbital periods $\lesssim 30$ hr, can also produce detectable radio emission, thus providing a means to identify Earth-sized extrasolar planets.

Key words: masers – radiation mechanism: non-thermal – stars: binaries: close – stars: white dwarfs – planetary systems – radio continuum: stars

1 INTRODUCTION

The operating requirements for electron-cyclotron masers are (i) a population inversion in the electron distribution and (ii) a magnetized plasma in which the electron-cyclotron frequency Ω_e exceeds the plasma frequency ω_p (e.g. Dulk 1985). The first condition can be achieved when the magnetic field geometry in the source region allows the development of an anisotropy in the electron distribution. One common example is the loss-cone electron distribution (e.g. Wu & Lee 1979), where an electron pitch-angle anisotropy develops within a magnetic flux tube with converging field lines at each footpoint. Large pitch angle electrons are magnetically reflected, whereas small-pitch-angle electrons are lost through collisions with high density plasma at the foot of the flux tube. The second condition is satisfied in magnetized plasmas with a relatively low electron density and/or high magnetic field strength.

These conditions are satisfied in a variety of astronom-

ical systems, including the solar corona (Melrose & Dulk 1982; Robinson 1991), terrestrial and planetary magnetospheres (Zarka 1992; Farrell, Desch & Zarka 1999; Ergun et al. 2000), and solar-like stars and magnetically-active binary stars (e.g. Melrose & Dulk 1982; Abada-Simon et al. 1994; Slee, Haynes & Wright 1994; Trigilio et al. 1998). Electron-cyclotron maser emission is characterized by high degrees of circular polarization (typically nearly 100%), high brightness temperatures ($T \gg 10^8$ K), and narrow beaming.

Planetary radio emissions are typically solar-wind driven, with the exception of a significant proportion of Jovian radio emissions, which are correlated with the orbital phase of Io (Bigg 1964), and to a lesser extent with the phases of Ganymede and Callisto (Menietti et al. 1998, 2001). In the unipolar-inductor model for the Jupiter-Io interaction (Piddington & Drake 1968; Goldreich & Lynden-Bell 1969) a current circuit is set up along the magnetic field lines connecting Io to Jupiter, closing in the Jovian ionosphere. The circuit is driven by the e.m.f. induced across Io, which is a conducting body, as it traverses the Jovian magnetic field. The existence of a Jupiter-Io current circuit was confirmed by the detection at ultraviolet and infrared

* E-mail: willes@physics.usyd.edu.au

† E-mail: kw@mssl.ucl.ac.uk

wavelengths of a footprint in Jupiter’s upper atmosphere, which remains fixed at the position of the footpoint of the Io flux tube as Jupiter rotates (Connerney et al. 1993; Clarke et al. 1996). The unipolar-inductor model predicts the existence of point-like auroral footprints. The observed tail of ultraviolet emission, extending up to 100° in longitude downstream of the bright Io footprint (Clarke et al. 2002), reveals that plasma-inertia effects are also important in the Jupiter-Io interaction, in addition to the unipolar inductor. The plasma-inertia effects are due to the presence of a dense plasma torus about Io’s orbit, consisting of ionized volcanic material from Io, which is “picked up” into corotation with the rotating Jovian magnetic field (Brown 1994). The auroral ultraviolet footprints for the Jovian moons Ganymede and Europa appear as point-like sources (Clarke et al. 2002), consistent with the unipolar-inductor model, despite the fact that the Ganymede-Jupiter interaction is complicated by Ganymede’s embedded magnetosphere (Kivelson et al. 1996). An auroral footprint for Callisto has not been detected because the footpoint of the Callisto flux tube is coincident with the main auroral oval (Clarke et al. 2002).

Radio emission is generated in the unipolar-inductor model by electron cyclotron maser emission from current-carrying electrons in the Io flux tube. The free energy for maser emission is provided by a loss-cone instability in the reflected electron velocity distribution. The observed anti-correlation between infrared footpoint emission and Io-controlled Jovian decametric radiation supports the hypothesis that the radio emission is driven by reflected electrons (Connerney et al. 1993). In addition, the negative frequency drifts evident in the fine-frequency structure of Jovian decametric radiation (the Jovian S-bursts) is consistent with maser emission driven by reflected electrons (Ellis 1974). Theoretical models based on electron-cyclotron maser emission can explain the observed high brightness temperatures ($\gtrsim 10^{17}$ K, Dulk 1970), 100% elliptical polarization (Dulk, Lecacheux & Leblanc 1992) and the radiation beaming pattern. Ground-based and dual spacecraft observations have confirmed the theoretical prediction that Io-controlled emission consists of hollow conical radiation beams, with opening angles $\lesssim 80^\circ$ and beam widths $\lesssim 2^\circ$, with the source location at the foot of the Io flux tube (Dulk 1967; Hewitt et al. 1981; Maeda & Carr 1992; Kaiser et al. 2000).

Recently, two ultra-short-period ($P < 10$ min) X-ray sources RX J1914+24 (Cropper et al. 1998; Ramsay et al. 2001, 2002b) and RX J0806+15 (Israel et al. 2002; Ramsay, Hakala & Cropper 2002a) were discovered. The remarkable characteristics of these sources are that there is only a single period for both the X-ray and optical emission, which is interpreted as the orbital period (Cropper et al. 1998) and the X-ray and optical emission are anti-phased (see Ramsay et al. 2001). The inferred orbital periods are too short to be from a binary system containing a white dwarf and a main-sequence star. Consequently, these X-ray sources are proposed to be compact binaries containing two white-dwarf stars, which may be in synchronous rotation with the orbit (Cropper et al. 1998). Their X-ray and optical/IR variations are contrary to those of typical accretion-powered sources, which often show multiple periods, corresponding to the orbital rotation, spin of the accreting star and beats. Moreover, the absence of optical polarization and helium emission lines

does not support the scenario involving mass transfer and accretion.

Wu et al. (2002) proposed a unipolar-inductor model to explain the peculiar X-ray and optical/IR variations of RX J1914+24, based on the unipolar-inductor model for the Jupiter-Io system. In the unipolar-inductor model for white-dwarf pairs, Jupiter is replaced by a magnetic white dwarf, and Io is replaced by a nonmagnetic white dwarf. The X-ray emission is powered by resistive heating of the magnetic white-dwarf atmosphere at the footpoints of the magnetic flux-tubes carrying the electric currents flowing between the white dwarfs. This is analogous to the ultraviolet footprint emission of the Galilean moons. The anti-phased optical/infrared emission emanates from the irradiated face of the nonmagnetic white dwarf, which is visible when the X-ray source is directed away from the observer. The orbital period gradually decreases in the unipolar-inductor model because the orbital evolution is driven by power losses through gravitational radiation, and is therefore consistent with timing measurements of the X-ray pulses from RX J1914+24, in which the orbital period decreases at a rate consistent with gravitational radiation losses (Strohmayer 2002). This is in contrast to models for the X-ray emission involving mass transfer from one white dwarf to another, which predict an increase in the orbital period. In contrast to the Jupiter-Io system, plasma-inertia effects are unlikely to be significant in the white-dwarf context because of the relatively high magnetic field strengths and low plasma densities (Wu et al. 2002).

It has also been proposed that unipolar induction can operate in isolated magnetic white-dwarf systems with terrestrial planets (Li, Ferrario & Wickramasinghe 1998). In this case the planet plays the role of the non-magnetic white dwarf in magnetic-nonmagnetic white-dwarf binary systems. The induced e.m.f. and dissipated power in the white-dwarf systems is significantly higher than in the planet-moon systems because the magnetic moment is higher for white dwarfs than for planets, and both white dwarfs and planets are typically larger than planetary moons.

We predict here, by direct analogy with the Jupiter-moon systems, that compact magnetic-nonmagnetic white-dwarf pairs and planets orbiting magnetic white dwarfs are strong electron-cyclotron maser sources. The large e.m.f. produced by the orbital motion of the system supplies high-energy electrons, and the (dipolar) geometry of the white-dwarf magnetic field and the low-plasma-density environment between the two stars or between the star and the planet can develop instabilities that generate electron-cyclotron maser emission.

Around 100 extrasolar planets are currently known. With the exception of pulsar planets, these planets, which have masses comparable to Jupiter and orbit around solar-like stars, were detected with the radial-velocity technique. Other methods proposed for detecting Jovian (gas-giant) planets around white dwarfs include observation of the excess thermal infrared emission associated with the Jovian planet (Ignace 2001; Burleigh, Clarke & Hodgkin 2002), or of re-emitted hydrogen recombination lines from the planetary atmosphere for close planetary orbits (\lesssim a few AU) around a hot white dwarf (Chu et al. 2001). We propose here that radio observations can reveal the presence of terrestrial planets in close orbits around white dwarf stars. These sys-

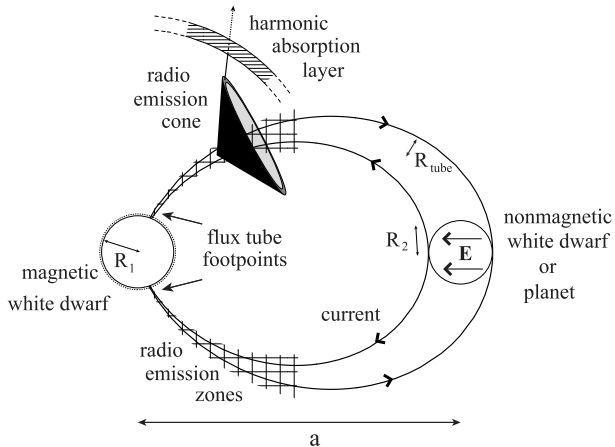


Figure 1. The unipolar-inductor model for white-dwarf pairs and white-dwarf planetary systems, where \mathbf{E} is the induced electric field across the nonmagnetic white dwarf or planet.

tems are remnants of main-sequence planetary systems in which terrestrial planets survive the stellar expansion phases and migrate to a stable close orbit around the white dwarf.

This paper is organized as follows. In §2 we use a simple model to calculate flux densities for maser emission, assuming parameters appropriate in the environment of white-dwarf pairs and of white-dwarf planetary systems. A more self-consistent consideration which takes into account the geometry and properties of the current sheets along the flux tubes will be presented in a future paper. In §3 we discuss briefly the astrophysical implications of the results obtained from our calculations.

2 MODEL OUTLINE

In this Section, we outline the model used to predict the flux densities for unipolar-inductor-driven radio emission in white-dwarf systems.

2.1 The unipolar-inductor current circuit

Figure 1 shows a schematic illustration of the unipolar-inductor model used in our calculation. For the magnetic-nonmagnetic white-dwarf pair, the system parameters are the magnetic white dwarf’s mass M_1 and magnetic moment μ , the non-magnetic white dwarf’s mass M_2 , and the binary period P . The radii of the magnetic and non-magnetic white dwarfs, R_1 and R_2 respectively, are obtained from the Hamada & Salpeter (1961) mass-radius relation (assuming helium white dwarfs), and the orbital separation a is calculated from the orbital period and the masses of the two white-dwarfs using Kepler’s third law. For the white-dwarf planetary system, the nonmagnetic white dwarf is replaced by a planet, and we use the same notation for the mass and radius (i.e. M_2 and R_2) for the planet. However, the planetary radius is treated as a free parameter instead of a quantity deduced from a mass-radius relation.

We define an asynchronism parameter ξ , which is the ratio of the spin angular speed of the magnetic white dwarf

to the orbital angular speed. In terms of the orbital parameters and the asynchronism parameter, the e.m.f. across the nonmagnetic white dwarf is

$$\Phi = \left(\frac{\mu_1 R_2}{c} \right) \left(\frac{2\pi}{P} \right)^{7/3} (1 - \xi) [G(M_1 + M_2)]^{-2/3} \quad (1)$$

(see Wu et al. 2002). For white-dwarf pairs with $P \approx 10$ min and $\mu_1 \sim 10^{32}$ G cm³, a seemingly small departure from synchronous rotation (e.g., $(1 - \xi) \sim 0.001$) can produce a sufficiently high e.m.f. to power X-ray emission at the magnetic footpoints with a luminosity a thousand times the solar bolometric luminosity.

Most of the electrical energy in magnetic-nonmagnetic white-dwarf pairs is dissipated in the flux tube footpoints at the surface of the magnetic white dwarf. This is because the cross-sectional area of the flux tube connecting the two white dwarfs at the footpoints is much smaller than the cross-sectional area at the nonmagnetic white dwarf. White-dwarf planetary systems will also dissipate most energy at the footpoints, provided that the conductivity of the planet is higher than the white-dwarf atmospheric conductivity. This condition is satisfied for a planetary body composed entirely of an Earth-like core, after the outer planetary layers have evaporated away at an earlier stage in the system’s evolution. In the case where a mantle layer is still present, the bulk of the electrical power would heat the planet if the mantle conductivity is lower than the white-dwarf atmospheric conductivity (Li et al. 1998). We consider only the case with an Earth-like planetary core in this study.

The effective resistance of the magnetic white dwarf at the footpoints of the flux tube is

$$\mathcal{R}_1 \approx \frac{1}{2\sigma_1 R_2} \left(\frac{a}{R_1} \right)^{3/2}, \quad (2)$$

(see Wu et al. 2002) where σ_1 is the white-dwarf atmospheric conductivity, and a is the orbital separation. The current flowing in the circuit is

$$I = \frac{\Phi}{\mathcal{R}_1}, \quad (3)$$

and is confined to a current sheet at the surface of the flux tube. The number density of current-carrying electrons n_{foot} at the footpoint is given by

$$n_{\text{foot}} = \frac{I}{e v A}, \quad (4)$$

where e is the electron charge, v is the average velocity of the current-carrying electrons, and A is the area of the arc-shaped footpoint. We can approximate A by

$$A \approx \pi \delta R_{\text{tube}}(R_1)^2, \quad (5)$$

where δ is the relative width of the current sheet, and $R_{\text{tube}}(R_1)$ is the flux-tube radius at the footpoint. Assuming a dipolar white-dwarf magnetic field, the flux-tube radius varies with distance r from the magnetic white dwarf as

$$R_{\text{tube}}(r) \approx R_2 \left(\frac{r}{a} \right)^{3/2}. \quad (6)$$

It follows that the number density of current-carrying electrons varies with distance as

$$n_c(r) \approx n_{\text{foot}} \left(\frac{R_1}{r} \right)^3. \quad (7)$$

Table 1. System parameters: mass M_2 and radius R_2 of the nonmagnetic white dwarf (first row) and planet (second and third rows), period P , asynchronicity parameter ξ , induced e.m.f. Φ , footpoint flux-tube radius $R_{\text{tube}}(R_1)$, and number density of current-carrying electrons at footpoint n_{foot} .

M_2 (M_\odot)	R_2 (cm)	P (hr)	ξ	Φ (statvolt)	$R_{\text{tube}}(R_1)$ (cm)	n_{foot} (cm^{-3}) ^a
0.5	9.6×10^8	0.14	0.999	4.0×10^4	2×10^7	1.7×10^{12}
1.2×10^{-6}	3.5×10^8	10	0	960	1.4×10^5	6.1×10^{12}
1.2×10^{-6}	3.5×10^8	28	0	88	5.0×10^4	1.6×10^{12}

^a assuming $\delta = 0.05$ rad and $v = 0.1c$

2.2 Formation of loss-cone electron distribution

As the downward-propagating, non-thermal, current-carrying electrons reach the polar footpoints, they are lost to collisions in the dense white-dwarf atmosphere. The dissipated electrical power produces the footpoint X-ray emission. We assume that collisional losses become significant at a height $0.01R_1$ above the white-dwarf surface, corresponding to the thickness of the white-dwarf atmosphere (e.g. Kippenhahn & Wiegert 1989).

Assuming adiabatic motion of electrons along the field lines, the electron speed is constant, together with the adiabatic invariant $\sin^2 \alpha / B$, where the electron pitch angle α is the angle between the velocity \mathbf{v} and the magnetic field \mathbf{B} . Higher up the flux tube (away from the footpoint), the precipitating electrons occupy the range of pitch angles $0 < \alpha < \alpha_{\text{lc}}$, with the critical angle α_{lc} given by

$$\alpha_{\text{lc}} = \sin^{-1} \left[\left(\frac{B}{B_f} \right)^{1/2} \right], \quad (8)$$

where B is the local magnetic field strength and B_f is the field strength at the footpoint. Thus the precipitating electrons map into a decreasing range of pitch angles with increasing distance from the footpoint. The other downward-propagating electrons with pitch angles $\alpha > \alpha_{\text{lc}}$ are reflected, before reaching the white-dwarf atmosphere, by a magnetic mirror formed by the converging field lines at the footpoint. Hence, the distribution of the reflected (upward-propagating) electrons at this position has a deficiency in electrons with pitch angles $\alpha < \alpha_{\text{lc}}$. This is the loss cone. The critical (loss-cone opening) angle α_{lc} decreases from $\pi/2$ rad, at the footpoint, with increasing distance along the flux tube.

The loss-cone distribution is modeled here with the Gaussian form:

$$f(v, \alpha) = f_0(v) F(\alpha), \quad (9)$$

with the velocity distribution

$$f_0(v) = \frac{n_{\text{lc}}}{(2\pi)^{2/3} m_e^3 V_{\text{lc}}^3} \exp\left(-\frac{v^2}{2V_{\text{lc}}^2}\right), \quad (10)$$

and the angular distribution

$$F(\alpha) = \begin{cases} 0 & \alpha < \alpha_{\text{lc}} - \Delta\alpha \\ 1 & \alpha > \alpha_{\text{lc}} \\ \Delta\alpha^{-1} [\alpha - (\alpha_{\text{lc}} - \Delta\alpha)] & \text{otherwise} \end{cases}, \quad (11)$$

where $\Delta\alpha$ is the loss-cone edge width, n_{lc} is the number density of loss-cone electrons, and $V_{\text{lc}} = (k_B T_{\text{lc}} / m_e)^{1/2}$ is the thermal-velocity spread for the loss-cone temperature T_{lc}

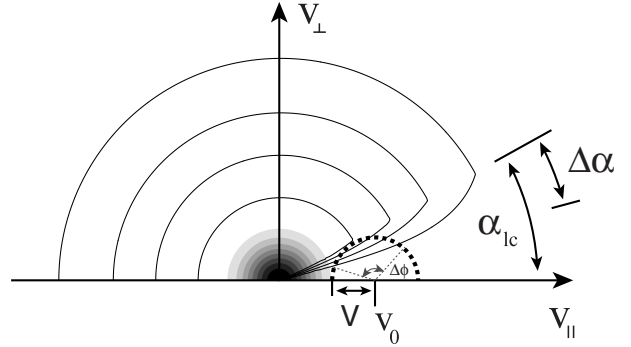


Figure 2. The loss-cone distribution is illustrated as contours in $v_{\parallel} - v_{\perp}$ space, where v_{\parallel} and v_{\perp} are the components of the velocity \mathbf{v} parallel and perpendicular to the magnetic field \mathbf{B} . The grayscale contours at low velocities correspond to the thermal background electron distribution, with number density n_{th} and temperature $T_{\text{th}} \ll T_{\text{lc}}$. A resonance circle (see Appendix A), with centre v_0 and radius V , is illustrated by a dashed line. The angle $\Delta\phi$ corresponds to the segment of the resonance circle which intersects the loss-cone edge.

(k_B is Boltzmann's constant). The loss-cone distribution is illustrated in Figure 2, as contours in $v_{\parallel} - v_{\perp}$ space (the components of \mathbf{v} parallel and perpendicular to \mathbf{B}). We note that our calculations assuming an idealized loss-cone distribution tend to overestimate the maser growth rate. In practice, the maser will operate close to a state of marginal stability due to competition between formation and maser-induced relaxation of the loss-cone instability (Robinson 1991). These considerations will be included in a more comprehensive model in a future paper.

We adopt the loss-cone instability in our model based on the following strong evidence for loss-cone-driven maser producing Io-controlled Jovian decametric radiation: (i) Connerney et al. (1993) reported an anti-correlation between the occurrence of Jovian decametric radiation and the presence of an infrared auroral footprint as a function of Jovian longitude. Radio emission is preferentially emitted at flux-tube footpoint longitudes with higher field strengths, where the magnetic mirror is more efficient. The field strength varies as a function of footpoint longitude due to the asymme-

tries in the tilted and non-centred Jovian magnetic field. At these longitudes a higher proportion of electrons are reflected, driving maser emission at the expense of precipitating electrons, which produce the footpoint emission. (ii) It is well established that the radiation pattern of Jovian decametric radiation is a hollow cone, with opening angle $\lesssim 80^\circ$ and beam width $\lesssim 2^\circ$ (Dulk 1967; Maeda & Carr 1992; Kaiser et al. 2000). This is consistent with the theoretical prediction for loss-cone driven masers (Hewitt et al. 1981).

We note that an alternative mechanism, where the maser instability is driven by a “shell” electron distribution, is also proposed to be relevant to astrophysical contexts (Ergun et al. 2000). The shell electron distribution, which drives Earth’s auroral kilometric radiation, is created by magnetic-field-aligned electric fields in the auroral zones. We argue that a shell maser is not applicable to Io-controlled Jovian radio emission because it produces a thin-disc radiation pattern, beamed exactly perpendicular to the magnetic field direction. It is unlikely that refraction or scattering can transform thin-disc beams into the observed hollow-cone beams, which have opening angles $\theta \lesssim 80^\circ$, and angular widths $\lesssim 2^\circ$. However, we cannot rule out the operation of the shell maser in white-dwarf systems. Nevertheless, the higher efficiency of the shell maser will produce higher flux densities than predicted by the loss-cone maser model adopted in this study, thereby improving the prospects for radio observation of white-dwarf systems.

2.3 Flux density spectra

Melrose & Dulk (1982) derived semi-quantitative expressions for the loss-cone-driven electron-cyclotron maser growth rate $\Gamma(\omega, \theta)$, emission bandwidth $\Delta\omega/\omega$ and angular spread $\Delta\theta$, as summarized in Appendix A. The wave modes generated by the electron-cyclotron maser depend most critically on the ratio ω_p/Ω_e in the source region (Hewitt, Melrose & Rönnmark 1981), where ω_p is the electron plasma frequency. The escaping wave modes (i.e., modes in which waves can escape from the source region to reach a distant observer) favoured by the electron-cyclotron maser are the fundamental and second-harmonic x -mode and the fundamental o -mode. The magnetoionic x -mode and o -mode have opposite senses of circular polarization. Higher harmonics have relatively low growth rates and are unlikely to grow to observable levels. In Appendix B we summarize the parameter ranges for these three modes in which the electron-cyclotron maser operates.

We estimate the peak brightness temperature in the source region by assuming saturation of the reactive version of the electron-cyclotron maser instability, i.e., where electron phase-bunching effects are significant. This assumption is made by analogy to Io-controlled Jovian decametric radio emissions, where the highest flux densities are attained by the subclass referred to as Jovian S-bursts, which exhibit properties consistent with phase-bunching effects (Carr & Reyes 1999; Willes 2002). A reactive growth mechanism saturates at wave amplitudes where electrons become trapped in the field of the growing waves. The saturation wave amplitude corresponds to where the trapping frequency ω_T becomes comparable with the growth rate, such that electrons

are trapped by the wave before they can contribute to wave growth. The trapping frequency is given by

$$\omega_T = \left(\frac{eEk}{m_e} \right)^{1/2}, \quad (12)$$

(Melrose 1986, p.70), where E is the wave electric field, and k is the wavenumber, with $k = \omega/c$ for waves with refractive index $n \approx 1$, which is valid for x -mode and o -mode waves sufficiently above their respective cutoff frequencies. The peak wave electric field E_{\max} can be obtained by equating the trapping frequency (Eq. 12) with the maser growth rate (Eq. A8), with

$$E_{\max} = \frac{m_e c \Gamma^2}{e \omega}. \quad (13)$$

It follows that the peak energy density

$$W = \frac{E_{\max}^2}{4\pi} = \frac{m_e^2 c^2 \Gamma^4}{4\pi e^2 \omega^2}. \quad (14)$$

The relation between brightness temperature T_b and energy density W in the source is

$$W = k_B T_b \left(\frac{\omega}{2\pi c} \right)^3 \left(\frac{\Delta\omega}{\omega} \right) \Delta\Omega \quad (15)$$

(Melrose & Dulk 1982), where $\Delta\omega/\omega$ is the bandwidth and $\Delta\Omega$ is the solid angle filled by the radiation, with $\Delta\Omega = 2\pi\Delta\cos\theta$. Using the derived expressions for the bandwidth (Eq. A12) and angular width (Eq. A13) of the loss-cone-driven maser, the brightness temperature

$$T_b = \frac{4\pi^2 c^6 W}{k_B \omega^3 v_0^3 \Delta\alpha^2 \cos^4 \alpha_{lc}}, \quad (16)$$

where v_0 is related to the emission angle θ in Equation (A7). The flux density S is related to the brightness temperature by

$$S = \left(\frac{\omega}{2\pi c} \right)^2 k_B \int d\Omega T_b \quad (17)$$

(Dulk 1985), where the integral is taken over the projected area of the source for the differential solid angle $d\Omega$. Assuming a constant brightness temperature over a source size equal to the flux tube radius R_{tube} , this simplifies to

$$S = \left(\frac{\omega}{2\pi c} \right)^2 k_B T_b \frac{\pi R_{\text{tube}}^2}{4d^2}, \quad (18)$$

where d is the distance to the source.

As the maser emission at harmonic number s , generated at a frequency $\omega = s\Omega_e$, propagates away from the magnetic white dwarf, it encounters harmonic absorption bands at $\omega \approx (s+1)\Omega_e, (s+2)\Omega_e, \dots$. The first absorption band is illustrated schematically in Figure 1. We incorporate harmonic damping effects in our calculations, using the approximate formula for the optical depth of the harmonic absorption bands in Appendix C.

3 RESULTS AND DISCUSSION

We consider three cases to illustrate the electron-cyclotron maser emission in white-dwarf systems. The first is a white-dwarf pair, and the other two are white-dwarf planetary systems with differing orbital periods. The system parameters of these three systems are listed in Table 1. In all cases, the

mass of the magnetic white dwarf M_1 is fixed to be $0.7 M_\odot$, its atmospheric conductivity σ_1 is 10^{14} s^{-1} , and its magnetic moment μ is 10^{31} G cm^3 . In the white-dwarf planetary systems, the spin of the white dwarf is not synchronized with the planetary orbit. We assume here that the spin period of the isolated magnetic white dwarf is significantly greater than the orbital period, and without loss of generality we set $\xi = 0$. The distances to all systems are fixed to be 100 pc. For the loss-cone parameters, unless otherwise stated, we assume that $\Delta\alpha = 0.05$, which corresponds to emission angular beam widths on the order of a few degrees (by analogy with the Jupiter-Io system), the loss-cone temperature $k_B T_{lc} = 1 \text{ keV}$ (where $1 \text{ eV} = 1.602 \times 10^{-12} \text{ erg}$) and the footpoint electron-number density $n_{lc} = 10^8 \text{ cm}^{-3}$. The loss-cone number density varies along the flux tube according to Equation (7). For these parameters we are assuming that only a very small fraction of current electrons ($\lesssim 0.01\%$) contribute to the loss-cone instability. Our flux density estimates are therefore conservative.

3.1 Magnetic-nonmagnetic white-dwarf pairs

3.1.1 Flux density spectra

Figure 3 shows the peak spectral flux densities for loss-cone-driven maser emission from a magnetic-nonmagnetic white-dwarf pair over a range of thermal plasma temperatures T_{th} and densities n_{th} . The binary system parameters are as shown in the first row of Table 1. We will discuss the dependence of the peak flux densities on T_{th} and n_{th} immediately below, and subsequently we discuss the dependence on the loss-cone parameters (temperature T_{lc} , electron number density n_{lc} and width $\Delta\alpha$).

At low thermal plasma densities ($n_{th} = 10^8 \text{ cm}^{-3}$; panels a and b), the maser operates in the fundamental x -mode over the entire displayed frequency range, up to the high-frequency cutoff (above 100 GHz) corresponding to the electron cyclotron frequency at the foot of the flux tube. Reabsorption of fundamental x -mode emission at the second harmonic layer (see Appendix C) becomes significant as the thermal temperature is increased. Consequently, the flux densities at low frequencies are much lower for $k_B T_{th} = 10 \text{ eV}$ than for $k_B T_{th} = 1 \text{ eV}$ (compare panels b and a in Figure 3).

At intermediate thermal plasma densities ($n_{th} = 10^9 - 10^{10} \text{ cm}^{-3}$; panels c, d, e and f), fundamental x -mode emission is suppressed at low frequencies (see Appendix B). The fundamental suppression frequency increases with increasing thermal plasma density, as indicated by the relative positions of the solid arrows in Figure 3, panels e and g. Note that there is a frequency overlap between fundamental and harmonic x -mode emission because the upper bound to harmonic emission is at twice the fundamental x -mode suppression frequency. The abrupt drop in flux density at high frequencies is due to thermal damping (see Appendix A, Equation (A16)).

At high thermal plasma densities ($n_{th} = 10^{11} \text{ cm}^{-3}$; panels g and h), the fundamental x -mode emission generated above the suppression frequency is strongly absorbed. Only the fundamental o -mode and the second harmonic x -mode emission generated below (twice) the suppression frequency

can escape to an observer. No escaping radiation is produced below $\sim 2.5 \text{ GHz}$, due to suppression of these modes.

The peak flux densities also vary with the loss-cone temperature T_{lc} . Figure 4 shows the flux density spectra for the same parameters as Figure 3, except with $k_B T_{lc} = 10 \text{ keV}$. The peak flux densities are consistently lower than in Figure 3, typically by four to five orders of magnitude. The dependence on the loss-cone electron number density is $S \propto n_{lc}^4$ (from Eqs. (A8), (14) and (16)). For example, increasing n_{lc} by a factor of ten, to 10^8 cm^{-3} , shifts all the flux density curves up by four orders of magnitude in Figures 3 and 4. The peak flux densities also decrease with increasing loss-cone width $\Delta\alpha$. For example, doubling the loss-cone width to $\Delta\alpha = 0.1 \text{ rad}$ lowers the flux density curves in Figures 3 and 4 by an order of magnitude.

3.1.2 Observability

We discuss here the observability of maser emission from white-dwarf pairs by adopting the parameters used in Figure 3 as an illustrative example. We consider two observing frequencies, 1.465 GHz and 43 GHz, which are available for the Very Large Array (VLA) radio telescope. We mark these frequencies by grey lines in Figure 3. In a recent search for radio emission from Jupiter-like extrasolar planets using the VLA, Bastian et al. (2000) considered a sensitivity limit of $0.02 - 0.07 \text{ mJy}$ at 1.465 GHz. We assume a sensitivity limit of 0.1 mJy ($1 \text{ Jy} = 10^{-23} \text{ erg cm}^{-2} \text{ s}^{-1} \text{ Hz}^{-1}$) at 1.465 GHz and 43 GHz in our discussion. This is a conservative estimate for the sensitivity at 43 GHz because the VLA sensitivity increases with observing frequency.

Maser emission would be detectable at 1.465 GHz for the following ranges of parameters. The fundamental x -mode emission is at least an order of magnitude above the detection threshold in panel a of Figure 3, and hence would be observed over the range of parameters: $n_{lc} \gtrsim 10^8 \text{ cm}^{-3}$, $k_B T_{th} \lesssim 1 \text{ eV}$, and $n_{th} \lesssim 10^8 \text{ cm}^{-3}$. At higher thermal densities, the fundamental x -mode emission is suppressed at this frequency (see panel c), and at higher thermal temperatures, the emission is strongly absorbed (see panel b), reducing the parameter range for observability to $n_{lc} \gtrsim 10^{10} \text{ cm}^{-3}$, $1 \lesssim k_B T_{th} \lesssim 10 \text{ eV}$, and $n_{th} \lesssim 10^8 \text{ cm}^{-3}$. The fundamental o -mode emission is detectable in the parameter range: $n_{lc} \gtrsim 10^{10} \text{ cm}^{-3}$, $k_B T_{th} \lesssim 10 \text{ eV}$, and $n_{th} \approx 10^{10} \text{ cm}^{-3}$ (panels e and f).

Note that for a loss-cone number density of $n_{lc} = 10^{10} \text{ cm}^{-3}$, corresponding to $\sim 1\%$ of current-carrying electrons in the loss-cone, the flux densities are eight orders of magnitude higher than those in Figures 3 and 4 (with $n_{lc} = 10^8 \text{ cm}^{-3}$). This is still a conservative estimate for the fraction of loss-cone electrons, considering that in the Jupiter-Io system the observed anti-correlation between footpoint emission and radio emission implies that a more significant fraction of the current-carrying electrons contribute to the loss-cone instability. No radio emission would be detected at 1.465 GHz for $n_{th} \gtrsim 10^{11} \text{ cm}^{-3}$, because all free space modes are suppressed at this frequency (panels g and h).

Maser emission would be detectable at 43 GHz over the following ranges of parameters. The fundamental x -mode emission is detectable for $n_{lc} \gtrsim 10^8 \text{ cm}^{-3}$, $k_B T_{th} \lesssim 10 \text{ eV}$, $n_{th} \lesssim 10^8 \text{ cm}^{-3}$ (panels a and b);

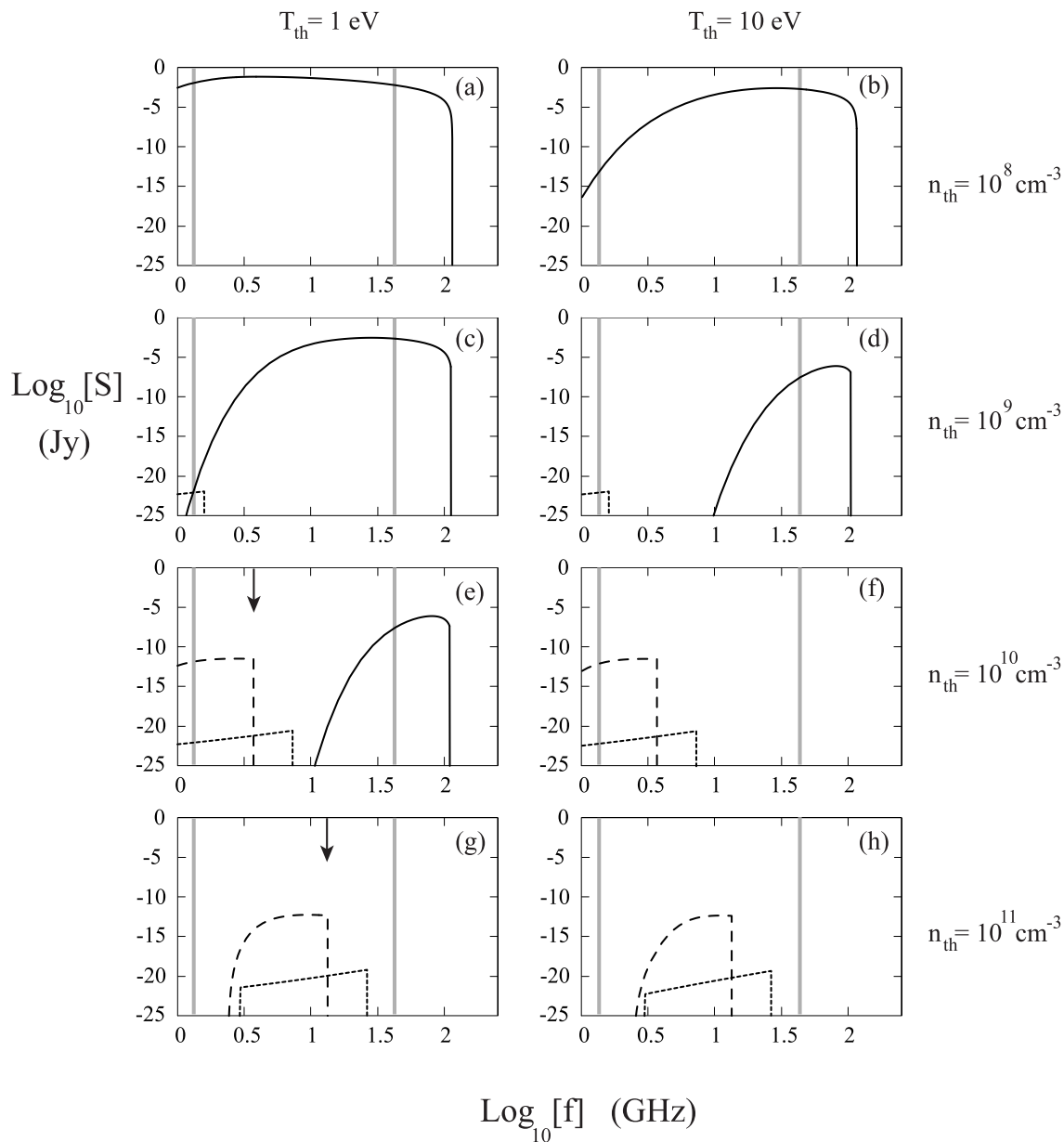


Figure 3. Peak spectral flux densities for radio emission from magnetic-nonmagnetic white-dwarf pairs (maximized over emission angle), with binary system parameters in Table 1. The loss-cone parameters are $k_B T_{lc} = 1$ keV, $n_{lc} = 10^8 \text{ cm}^{-3}$, and $\Delta\alpha = 0.05$ rad. Two values are considered for the thermal plasma temperature, with $k_B T_{th} = 1$ eV (panels a, c, e and g in the left column) and $k_B T_{th} = 10$ eV (panels b, d, f and h in the right column); four values are considered for the thermal plasma density, with $n_{th} = 10^8 \text{ cm}^{-3}$ (panels a and b), $n_{th} = 10^9 \text{ cm}^{-3}$ (panels c and d), $n_{th} = 10^{10} \text{ cm}^{-3}$ (panels e and f), and $n_{th} = 10^{11} \text{ cm}^{-3}$ (panels g and h). Spectral density profiles for the fundamental x -mode (solid line), the fundamental o -mode (dashed line), and the second harmonic x -mode (dotted line) are displayed. The vertical grey bars denote VLA observation frequencies at 1.465 GHz and 43 GHz.

$n_{lc} \gtrsim 10^8 \text{ cm}^{-3}$, $k_B T_{th} \lesssim 1$ eV, $10^8 \lesssim n_{th} \lesssim 10^9 \text{ cm}^{-3}$ (panel c); $n_{lc} \gtrsim 10^9 \text{ cm}^{-3}$, $1 \lesssim k_B T_{th} \lesssim 10$ eV, $10^8 \lesssim n_{th} \lesssim 10^9 \text{ cm}^{-3}$ (panel d); and $n_{lc} \gtrsim 10^9 \text{ cm}^{-3}$, $k_B T_{th} \lesssim 1$ eV, $10^9 \lesssim n_{th} \lesssim 10^{10} \text{ cm}^{-3}$ (panel e).

Second-harmonic x -mode emission is only relevant in a small region of parameter space (for $n_{th} \approx 10^{11} \text{ cm}^{-3}$ in panels g and h, in the frequency range 13–26 GHz. A large fraction ($\gtrsim 50\%$) of current-carrying electrons must contribute

to the loss cone (corresponding to $n_{lc} \gtrsim 10^{12} \text{ cm}^{-3}$) in order for second harmonic emission to be detected. We therefore conclude that second harmonic maser emission only plays a marginal role in radio emission from white dwarf systems.

The predicted radio flux at the Earth from white-dwarf pairs is variable, with zero flux when the emission cone is not directed towards the observer. For emission cone widths of several degrees, the duty cycle is on the order of one percent. Thus, for the white-dwarf pair parameters assumed above,

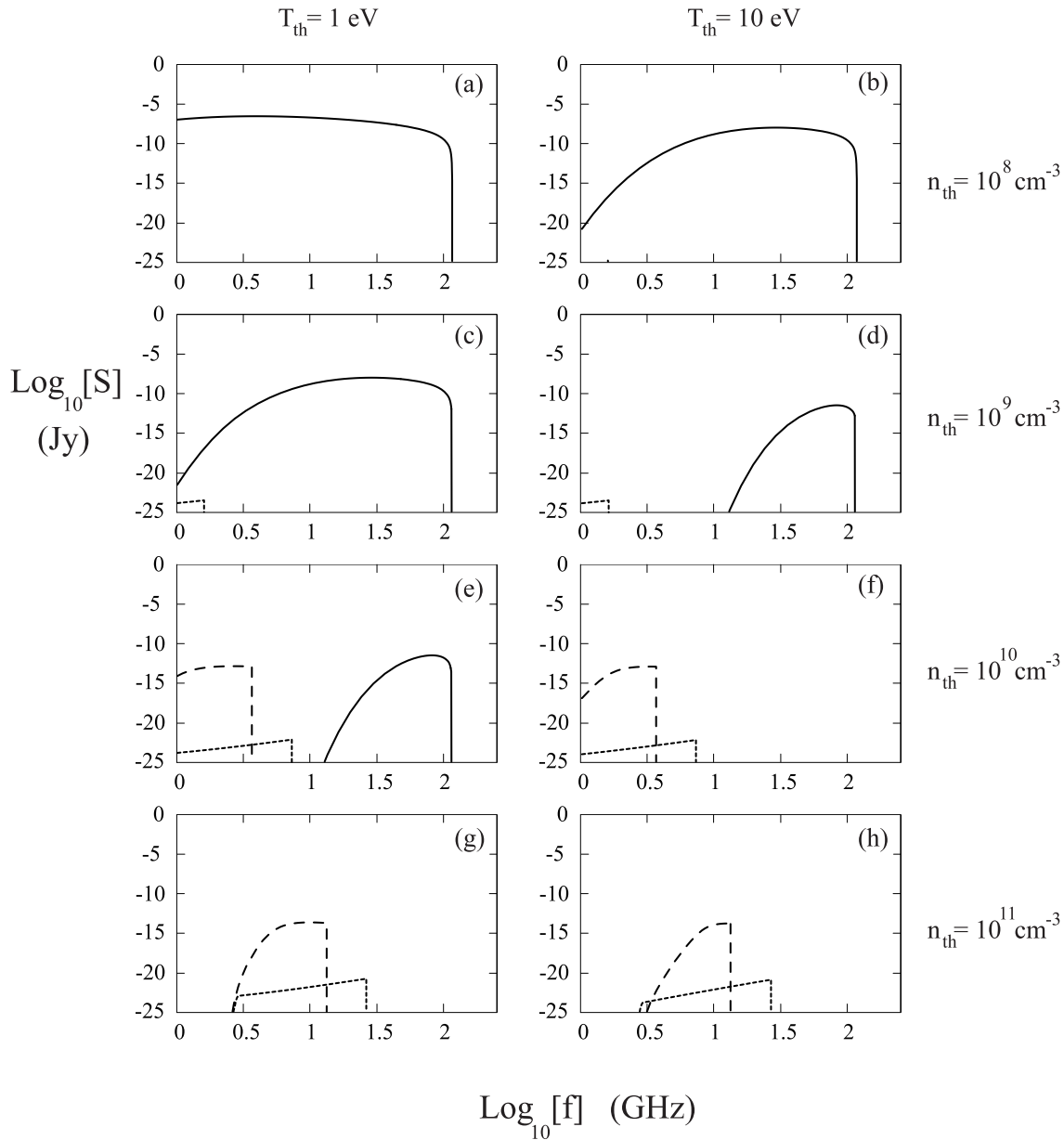


Figure 4. Peak spectral flux densities for radio emission from magnetic-nonmagnetic white-dwarf pairs for same parameters as Figure 3, except with a higher loss-cone plasma temperature: $k_B T_{lc} = 10$ keV.

with $P = 500$ s, the radio pulses have durations of $\gtrsim 5$ seconds. The interval between pulses is equal to the orbital period P for the extreme viewing geometry where one edge of the emission cone grazes the line-of-sight at one point in the orbit. More generally, an emission cone with opening angle θ will intersect the line-of-sight at two points per orbit, and within each orbital cycle the two pulses are separated by an interval with a value between zero and $P\theta/\pi$, depending on the viewing geometry of the system.

3.1.3 Unipolar inductor lifetimes

An important constraint to the probability of detection for white-dwarf pairs is the lifetime of the unipolar-inductor phase and the binary lifetime. The duration of the unipolar-inductor phase is related to the rate of synchronization between the magnetic white-dwarf spin and the orbital rotation, due to Lorentz torques associated with the energy dissipation in the current circuit (see Wu et al. 2002). For the parameters assumed here, this timescale is $\sim 10^4$ yr. The binary lifetime is determined by gravitational radiation power losses and is $\sim 10^6$ yr. Hence, the probability of detecting close white-dwarf pairs in the unipolar-inductor phase is $\sim 1\%$. Despite the low probability of detection, two systems

RX J1914+24 (Cropper et al. 1998; Ramsay et al. 2001, 2002b) and RX J0806+15 (Israel et al. 2002; Ramsay et al. 2002a) with ultra-short periods ($P < 10$ min), are candidate unipolar-inductor white-dwarf pairs and are also potential maser sources. If these systems are indeed ultra-short period white-dwarf pairs powered by unipolar induction, their discoveries suggest that there is either an abundant population of such close white-dwarf pairs in the Galaxy, or that the unipolar-inductor phase may be longer than the above estimate of $\sim 1\%$ of the system lifetime. The latter possibility may be due to a close white-dwarf pair entering the unipolar-inductor phase multiple times; for instance, if a (post-unipolar-inductor) synchronous system undergoes intermittent mass exchange that breaks the synchronism and initiates a new unipolar-inductor phase.

3.2 White-dwarf planetary systems

White-dwarf planetary systems consisting of a magnetic white dwarf and an Earth-like core with orbital separation of 1 AU ($\sim 2 \times 10^4 R_1$) have orbital periods ~ 1 yr. The components in these systems are too far apart for the induced e.m.f. across the planetary core to be sufficiently large to accelerate fast (keV) electrons. Masers operate more efficiently in more compact systems which are more effective unipolar inductors. Here we consider only compact white-dwarf planetary systems with orbital periods $P \approx 10 - 30$ hr (see Table 1). We first discuss the properties of the maser emission from these systems and then other aspects, such as the formation scenario and lifespan of close white-dwarf planetary systems.

3.2.1 Emission properties

The principle of maser operation in white-dwarf planetary systems is very similar to the white-dwarf pairs discussed above. The dependence of the emission properties on the loss-cone parameters are qualitatively the same, after rescaling the system parameters (period and masses) accordingly. For systems comprising an Earth-sized planetary core orbiting a non-spinning magnetic white dwarf, an orbital period of ~ 10 hr corresponds to an orbital separation of $\sim 200 R_1$ ($\sim 2 R_\odot$). As shown in Table 1, the induced e.m.f. in these systems is about 40 times smaller than for the close white-dwarf pairs discussed in § 3.1 but is comparable to the induced e.m.f. in the Jupiter-Io circuit, which accelerates keV electrons. Moreover, because the size of the planetary core is two orders of magnitude smaller than the size of the non-magnetic white dwarf, the footpoint radius of the current flux tubes, and hence the maser source size, is greatly reduced in the white-dwarf planetary systems.

We show in Figure 5 the flux density spectra for maser emission from a white-dwarf planetary system with $P = 10$ hr. The predicted flux densities are typically four orders of magnitude lower than for the white-dwarf pair systems in § 3.1. The parameter ranges for which radio emission is detectable with the VLA are reduced from those quoted in § 3.1.2, with the minimum values of n_{lc} multiplied by a factor of ten (which increases the peak flux densities by four orders of magnitude).

The peak flux densities decrease as the orbital separa-

tion increases. For instance, by doubling the orbital separation (corresponding to the system parameters in the third row of Table 1), the induced e.m.f. is an order of magnitude lower, but is comparable to the induced e.m.f. in the Jupiter-Callisto circuit, which generates radio emission of comparable power to the Jupiter-Io circuit (Menietti et al. 2001). The peak flux densities (not shown) are, on average, an order of magnitude lower than in Figure 5; again, the decrease is predominantly due to the smaller source size at the foot of the flux tube.

3.2.2 Lifetimes and formation scenario

Whether or not we can detect maser emission from white dwarf planetary systems depends not only on the emission properties of the systems but also the number of systems and the proportion of the planetary-system lifespan occupied by the unipolar-inductor phase. The lifetime of the unipolar-inductor phase is limited by the inward drift of the planet due to Lorentz torques. The inward drift speed is estimated to be (Li et al. 1998)

$$v_{\text{drift}} = -\frac{4\Phi I a^2}{GM_1 M_2}. \quad (19)$$

The characteristic lifetime of the white-dwarf planetary system, $\tau \approx a/v_{\text{drift}}$, scales with binary period as $\tau \propto P^5$ and with magnetic moment as $\tau \propto \mu^{-2}$. The 10-hr and 28-hr period systems considered above thus have lifetimes of $\sim 10^7$ and 10^9 yr respectively. In general, the probability of observing a white dwarf planetary system in the unipolar-inductor phase increases with the binary period P . This trend is offset by the decrease in the induced e.m.f. and maser flux density with increasing P . Increasing the white dwarf magnetic moment increases the induced e.m.f. and footpoint dissipation, but simultaneously reduces the unipolar inductor lifetime. For example, if we increase the magnetic moment by a factor of 10, to $\mu_1 = 10^{32} \text{ G cm}^3$ for the 28 hour system, the lifetime will decrease from 10^9 yr to 10^7 yr.

There is firm observational evidence for the existence of double degenerate white-dwarf systems and of isolated magnetic white dwarfs. Given that the low-mass companion stars in AM Her type binaries and in intermediate polars (see e.g. Cropper 1990; Warner 1995) will eventually become degenerate, the existence of magnetic-nonmagnetic white-dwarf pairs is very likely. However, the existence of white-dwarf planetary systems is far less certain. We now briefly discuss whether solar-like stellar planetary systems could evolve into the maser-emitting white-dwarf planetary systems investigated theoretically here.

Solar-type stars undergo two major expansions towards the end of their lives — the first occurs as they reach the Red Giant Branch (RGB), and the second occurs on the Asymptotic Giant Branch (AGB) at the end of the core helium burning. The AGB phase is characterized by multiple thermal pulses caused by nuclear instabilities in the helium-burning shell. In each thermal pulse, the stellar radius expands by approximately 25% and contracts over short timescales (Sackmann et al. 1993). Following the AGB phase, the star rapidly contracts and eventually becomes a white dwarf.

The expansion phases of a solar-type star have crucial effects on the fate of their orbiting planets. There are three

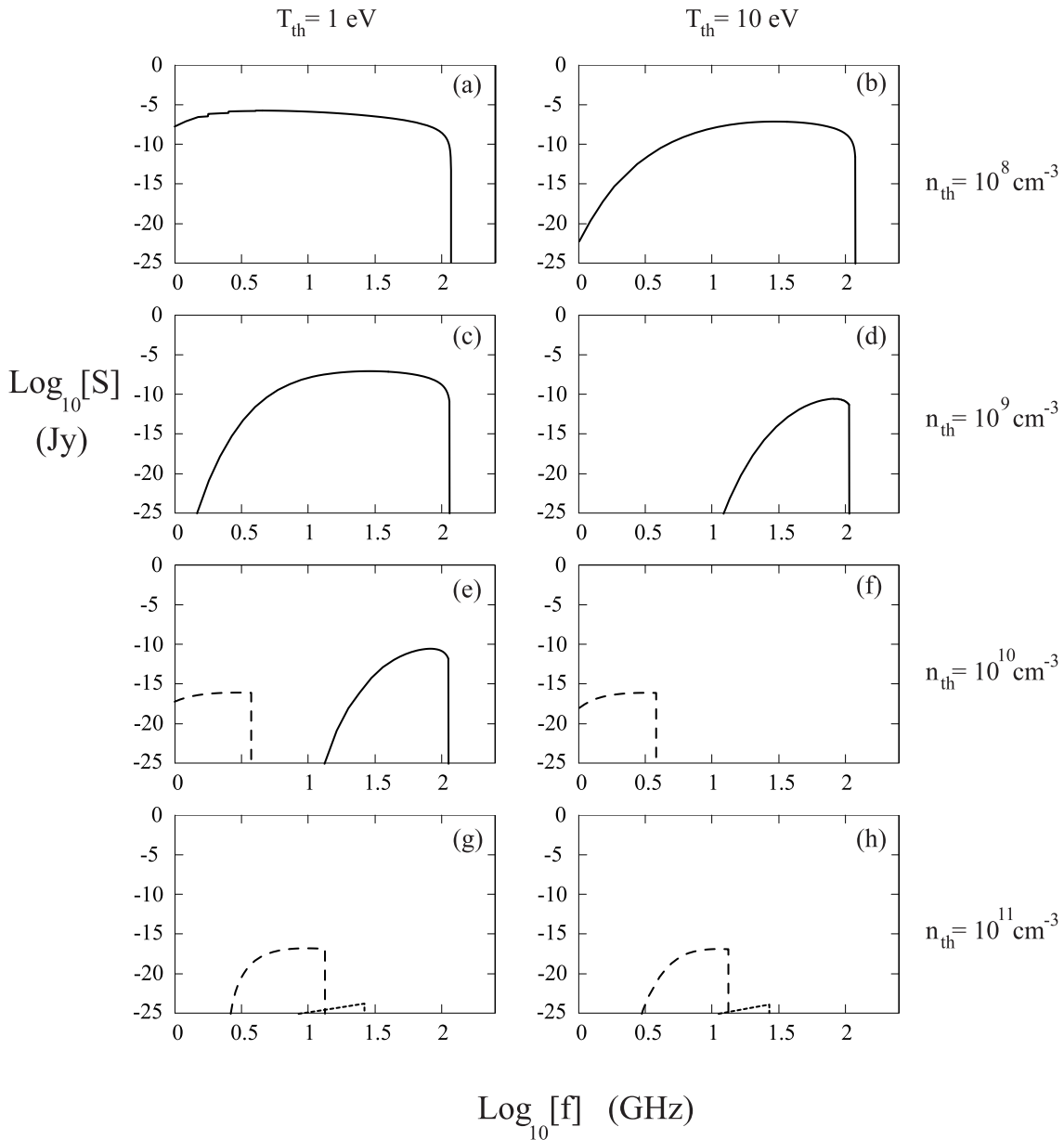


Figure 5. Peak spectral flux densities for radio emission from an Earth-sized planetary core orbiting a magnetic white dwarf (maximized over emission angle) for two values of thermal plasma temperature ($k_{\text{B}}T_{\text{th}} = 1$ eV for panels a, c, e, g; $k_{\text{B}}T_{\text{th}} = 10$ eV for panels b, d, f, h), and four values of thermal plasma density ($n_{\text{th}} = 10^8 \text{ cm}^{-3}$ for panels a and b; $n_{\text{th}} = 10^9 \text{ cm}^{-3}$ for panels c and d; $n_{\text{th}} = 10^{10} \text{ cm}^{-3}$ for panels e and f; $n_{\text{th}} = 10^{11} \text{ cm}^{-3}$ for panels g and h). The orbital parameters are shown in second row in Table 1. The loss-cone parameters are $k_{\text{B}}T_{\text{lc}} = 1$ keV, $n_{\text{lc}} = 10^8 \text{ cm}^{-3}$ and $\Delta\alpha = 0.05$. Spectral density profiles for fundamental x -mode (solid line), fundamental o -mode (dashed line), and the second harmonic x -mode (dotted line) are displayed.

likely scenarios: (i) Engulfment: If the expanding stellar radius exceeds the orbital separation during the RGB phase or the AGB phase (excluding thermal pulses), the planet will evaporate. (ii) Temporary engulfment: This is when the stellar radius intermittently exceeds the orbital separation during the thermal pulses in the AGB phase. The planet lies within the stellar envelope for a short period (between 10^2 and 10^3 yr) and is only partially evaporated (Sackmann et al. 1993; Rybicki & Denis 2001). During the temporary engulfment, the dominant force is the “bow-shock” drag,

which causes the planet to spiral inwards. (iii) Otherwise, two competing effects determine the evolution of the planetary orbits. The first is that the orbital separation increases due to mass loss from the star in the giant phase (Sackmann et al. 1993). The second effect is that tidal drag forces (through which the orbital angular momentum of the planet is transferred to the stellar envelope) become significant as the stellar radius approaches the orbital separation. The tidal interaction acts to decrease the orbital separation, and

it dominates over stellar-mass-loss effects when the stellar radius expands beyond a threshold value.

A prediction for the fate of solar system planets, based on various existing solar evolution models (Rybicki & Denis 2001), is that the planets at a greater distance from the Sun than Mars will all migrate out due to stellar-mass-loss effects. Mars is beyond reach of the expanded red-giant envelope of the Sun, and the tidal interaction is negligible; so it will not spiral in. Mercury and Venus will spiral in and evaporate. The fate of the Earth is less certain, depending on the assumed solar evolutionary model. Rybicki & Denis (2001) estimated the spiral-in distance for the Earth in the temporary engulfment scenario to be $(10 - 70) R_{\odot}$ per thermal pulse, and predicted that the Earth can survive several thermal pulses before being permanently engulfed. The survival probability increases with the assumed mass-loss rate during the RGB phase in the evolutionary model because the number of thermal pulses in the AGB phase is reduced (Sackmann et al. 1993). Clearly, even with uncertainties in the precise evolutionary behaviour of the star, there can still exist a range of initial orbital separations from which terrestrial planets migrate to very small final orbital separations at the end of the AGB phase, through a combination of temporary engulfment and tidal interaction effects.

According to this scenario, the parameter space for the formation of close white-dwarf planetary systems is narrow, and we should not anticipate a large fraction of main-sequence planetary systems with terrestrial planets evolving to the compact white-dwarf planetary systems that allows efficient unipolar induction to occur, producing strong maser emission. The evolutionary scenario discussed above has not taken into account the drift-in effects due to the Lorentz torque (see Li et al. 1998). Nevertheless, detailed modeling of the planet-star interaction with correct treatments of stellar evolution, hydrodynamics and magnetic interaction are necessary to estimate this fraction.

4 SUMMARY

We propose that magnetic-nonmagnetic white dwarf pairs with short orbital periods $\lesssim 10$ min, and planetary systems comprising a magnetic white dwarf and an Earth-sized planetary core with orbital periods $\lesssim 30$ hr are strong, periodically variable, and highly polarized radio sources. The radio emission is generated by electron cyclotron maser emission in a unipolar-inductor current circuit driven by the asynchronicity between the spin of the magnetic white dwarf and the orbital motion of the nonmagnetic white dwarf or planet. This model is a direct analogy to Jovian radio emissions generated in conjunction with the Galilean moons.

We apply a simple model to predict the flux densities of the radio emission for the two polarization modes received at the Earth from white-dwarf maser systems, assuming a source distance of 100 pc. Other model assumptions include a dipolar magnetic field for the magnetic white dwarf, and a constant thermal plasma density in the immediate vicinity of the binary system. The free parameters in the model are the binary system parameters (component masses and radii, orbital distance and period), the thermal plasma parameters (density and temperature), and loss-cone parameters (density, temperature, and loss-cone width) for the elec-

trons which are accelerated in the flux tube current circuit connecting the two components.

Our conclusions for magnetized-unmagnetized white dwarf pairs are as follows. (1) White dwarf pairs with orbital periods $\lesssim 10$ min are strong radio sources over a broad range of free parameters in the model. (2) The frequency range of radio emission in various wave modes is determined by the primary white dwarf's magnetic moment and the thermal plasma density. (3) The radio emission spectrum can be discontinuous, and the two polarization modes (with opposite senses of circular polarization) may be detected at different frequencies. (4) The detection probability is limited by the lifetime of the unipolar inductor phase relative to the binary lifetime. (5) The predicted radio emission is periodic following the orbital motion of the system, with the duty cycle depending on the width of the hollow-cone emission beam.

Our conclusions for white-dwarf planetary systems are as follows. (1) Earth-sized planetary cores orbiting magnetic white dwarfs with orbital periods $\lesssim 30$ hr are strong radio sources, but over a more limited range of parameters than for white-dwarf pairs. (2) Electrical dissipation in the unipolar inductor circuit causes the planet to gradually drift in towards the white dwarf. White-dwarf planetary systems have a significantly longer unipolar-inductor phase than white-dwarf pairs. (3) The longer orbital period for white-dwarf planetary systems (in comparison to white dwarf pairs) implies longer pulse times: the pulse timescale is about tens of minutes, with pulse separation about tens of hours (compared with the pulse timescales of a few seconds and pulse separation of a few minutes for white-dwarf pairs). (4) Only a small fraction of main-sequence-star planetary systems containing terrestrial planets evolve to close-orbit white-dwarf planetary systems which produce maser emission. Nevertheless, the large number of galactic white dwarfs increases the detection probability.

ACKNOWLEDGMENTS

We thank Zdenka Kuncic, Don Melrose, Peter Robinson, and Mike Wheatland for comments and critically reading the manuscript. AJW acknowledges support from the Australian Research Council through an ARC Postdoctoral Research Fellowship.

REFERENCES

- Abada-Simon M., Lecacheux A., Louarn P., Dulk G.A., Belkora L., Bookbinder J.A., Rosolen C., 1994, *A&A*, 288, 219
- Bastian T.S., Dulk G.A., Leblanc Y., 2000, *ApJ*, 545, 1058
- Bigg E.K., 1964, *Nature*, 203, 1008
- Brown M.E., 1994, *Geophys. Res. Lett.*, 21, 847
- Burleigh M.R., Clarke F.J., Hodgkin S.T., 2002, *MNRAS*, 331, L41
- Carr T.D., Reyes F., 1999, *J. Geophys. Res.*, 104, 25127
- Connerney J.E.P., Baron R., Satoh T., Owen T., 1993, *Science*, 262, 1035
- Chu Y-H, Dunne B.C., Gruendl R.A., Brandner W., 2001, *ApJ*, 546, L61
- Cropper M., 1990, *Space Sci. Rev.*, 54, 195
- Cropper M., Harrop-Allin M.K., Mason K., Mittaz J.P., Potter S.B., Ramsay G., 1998, *MNRAS*, 293, L57
- Dulk G.A., 1967, *Icarus*, 7, 173

- Dulk G.A., 1970, ApJ, 159, 671
Dulk G.A., 1985, ARA&A, 23, 169
Dulk G.A., Lecacheux A., Leblanc Y., 1992, A&A, 253, 292
Ellis G.R.A., 1974, Proc. Astron. Soc. Aust., 2, 236
Ergun R.E., Carlson C.W., McFadden J.P., Delory G.T., Strangeway R.J., Pritchett P.L., 2000, ApJ, 538, 456
Farrell W.M., Desch M.D., Zarka, P., 1999, J. Geophys. Res., 104, 14025
Goldreich P., Lynden-Bell D., 1969, ApJ, 156, 59
Hamada T., Salpeter E., 1961, ApJ, 134, 683
Hewitt R.G., Melrose D.B., Rönmark K.G., 1981, Proc. Astron. Soc. Aust., 4, 221
Ignace R., 2001, Publ. Astron. Soc. Pac., 113, 1227
Israel G.L., et al., 2002, A&A, 386, L13
Kaiser M.L., Zarka P., Kurth W.S., Hospodarsky G.B., Gurnett D.A., 2000, J. Geophys. Res., 105, 16053
Kippenhahn R., Wiegert A., 1989, Stellar Structure and Evolution, Springer-Verlag, Berlin, p.375
Kivelson M.G., Khurana K.K., Russell C.T., Walker R.J., Warnecke J., Coroniti F.V., Polansky C., Southwood D.J., Schubert G., 1996, Nature, 384, 537
Kuncic Z., Robinson P.A., 1993, Solar Phys., 145, 317
Li J., Ferrario L., Wickramasinghe D.T., 1998, ApJ, 503, L151
Maeda K., Carr T.D., 1992, J. Geophys. Res., 97, 1549
Melrose D.B., 1980, Plasma Astrophysics, Vol. 2, Gordon & Breach, Dordrecht
Melrose D.B., 1986, Instabilities in Space and Laboratory Plasmas, Cambridge University Press, Cambridge
Melrose D.B., 1991, ApJ, 380, 256
Melrose D.B., Dulk G.A., 1982, ApJ, 259, 844
Menietti J.D., Gurnett D.A., Kurth W.S., Groene J.B., 1998, Geophys. Res. Lett., 25, 4281
Menietti J.D., Gurnett D.A., Christopher I., 2001, Geophys. Res. Lett., 28, 3047
Piddington J.H., Drake J.F., 1968, Nature, 217, 935
Ramsay G., Cropper M., Wu K., Mason K., Hakala P., 2001, MNRAS, 311, 75,
Ramsay G., Hakala P., Cropper M., 2002a, MNRAS, 332, L7
Ramsay G., Wu K., Cropper M., Schmidt G., Sekiguchi K., Iwamura F., Maihara T., 2002b, MNRAS, 333, 575
Robinson P.A., 1991, Solar Phys., 134, 299
Rybicki K.R., Denis C., 2001, Icarus, 151, 130
Sackmann I.-J., Boothroyd A.I., Kraemer K.E., 1993, ApJ, 418, 457
Slee O.B., Haynes R.F., Wright A.E., 1984, MNRAS, 208, 865
Strohmayr T.E., 2002, ApJ, in press
Triglio C., Leto P., Umama G., 1998, A&A, 330, 1060
Warner D., 1995, Cataclysmic Variable Stars, Cambridge University Press, Cambridge
Willes A.J., Robinson P.A., 1996, ApJ, 467, 465
Willes A.J., 2002, J. Geophys. Res., 107, 10.1029/2001JA000282
Wu C.S., Lee L.E., 1979, ApJ, 231, 621
Wu K., Cropper M., Ramsay G., Sekiguchi K., 2002, MNRAS, 331, 221
Zarka P., 1992, Adv. Space Res., 12, 99

APPENDIX A: ELECTRON-CYCLOTRON MASER GROWTH RATE

In a magnetized plasma, the resonance condition between waves and electrons is

$$\omega - \frac{s}{\gamma} \Omega_e - k_{\parallel} v_{\parallel} = 0, \quad (\text{A1})$$

where s is the harmonic number, Ω_e is the electron cyclotron frequency, and k_{\parallel} and v_{\parallel} are the components of the wavevector and velocity parallel to \mathbf{B} . Assuming the semi-relativistic

approximation (see Wu & Lee 1979), the Lorentz factor simplifies to

$$\gamma = 1 + \frac{v_{\parallel}^2}{2c^2} + \frac{v_{\perp}^2}{2c^2}, \quad (\text{A2})$$

and the resonance condition traces out a circle in the $v_{\parallel} - v_{\perp}$ space (see Fig. 2), with centre on the v_{\parallel} -axis

$$v_0 = \frac{k_{\parallel} c^2}{\omega}, \quad (\text{A3})$$

and radius

$$V = c \left[\frac{k_{\parallel}^2 c^2}{\omega^2} - \frac{2(\omega - s\Omega_e)}{s\Omega_e} \right]^{1/2}. \quad (\text{A4})$$

The electron-cyclotron maser growth rate for harmonic s and wave mode σ (with $\sigma = -1$ for x -mode waves and $\sigma = 1$ for o -mode waves) is given by

$$\Gamma_{s,\sigma}(\mathbf{k}) = \int d^3\mathbf{p} A_{s,\sigma}(\mathbf{p}, \mathbf{k}) \delta(\omega - s\Omega_e/\gamma - k_{\parallel} v_{\parallel}) \quad (\text{A5}) \\ \times \left(\frac{s\Omega_e}{\gamma v_{\perp}} \frac{\partial}{\partial p_{\perp}} + k_{\parallel} \frac{\partial}{\partial p_{\parallel}} \right) f(\mathbf{p})$$

with

$$A_{s,\sigma}(\mathbf{p}, \mathbf{k}) = \frac{4\pi^2 e^2 c^2 \beta_{\perp}^2}{\omega n_{\sigma} (1 + T_{\sigma}^2) \partial(\omega n_{\sigma})/\partial\omega} \quad (\text{A6}) \\ \times \left| \frac{K_{\sigma} \sin\theta + (\cos\theta - n\beta_{\parallel}) T_{\sigma}}{n_{\sigma} \beta_{\perp} \sin\theta} J_s(z) + J'_s(z) \right|^2$$

(Melrose 1980; Melrose & Dulk 1982), where T_{σ} , K_{σ} , and n_{σ} are the axial ratio, longitudinal polarization and refractive index for wave mode σ , $J_s(z)$ is the Bessel function of the first kind (order s) and $J'_s(z)$ is its derivative. The argument of the Bessel function $z = \omega n_{\sigma} \beta_{\perp} \sin\theta/\Omega_e$; and the velocity component $(\beta_{\perp}, \beta_{\parallel}) = (v_{\perp}, v_{\parallel})/c$. The resonance condition appears as the argument in the δ -function in Equation (A6), and the growth rate is evaluated as a line integral over the resonance circle. The conditions for driving a perpendicular-driven maser (with $\partial f/\partial p_{\perp} > 0$ on the resonance circle) are therefore satisfied for the loss-cone electron distribution modeled by Equation (9).

Melrose and Dulk (1982) derived a semi-quantitative approximation for the maximum loss-cone maser growth rate, where for a given loss-cone angle α_{lc} , and resonance circle centre v_0 , the maximum growth rate corresponds to the resonance circle which touches the inside edge of the loss cone, with radius $V = v_0 \sin\alpha_{lc}$. For x -mode waves sufficiently above the cutoff frequency of the mode, the refractive index $n \approx 1$, and the resonance circle centre is related to the wave angle θ , with

$$v_0 = c \cos\theta. \quad (\text{A7})$$

The maximum growth rate is

$$\Gamma_{s,\sigma} = \frac{2\pi m_e^2 c^2 A_{s,\sigma} f_0(v_0 \cos\alpha_{lc})}{v_0} \frac{\Delta\phi(\alpha_{lc}, \Delta\alpha)}{\Delta\alpha}, \quad (\text{A8})$$

where $\Delta\phi$ corresponds to the portion of the resonance circle which passes through the loss-cone edge, as illustrated in Figure 2, with

$$\Delta\phi(\alpha_{lc}, \Delta\alpha) = \pi - 2 \sin^{-1} \left(\frac{\sin(\alpha_{lc} - \Delta\alpha)}{\sin\alpha_{lc}} \right), \quad (\text{A9})$$

and

$$A_{s,\sigma} = \frac{\pi \omega_p^2 m_e v_0^2 \sin^2 \alpha_{lc} \cos^2 \alpha_{lc} a_s (1 + v_0 \sin^2 \alpha_{lc} T_\sigma / c)^2}{4 \omega n_e (1 + T_\sigma^2)} \times \left(\frac{v_0 \sin \alpha_{lc} \cos \alpha_{lc}}{c} \right)^{2s-2} \left(1 - \frac{v_0^2}{c^2} \right)^{s-1}, \quad (\text{A10})$$

where $a_s = 4s^{2s} / [2^{2s} (s!)^2] = 1$ for $s = 1, 2$. The maximum growth rate occurs at frequency $\omega_{\max,s}$, given by

$$\omega_{\max,s} = s \Omega_e \left(1 + \frac{v_0^2 \cos^2 \alpha_{lc}}{2c^2} \right). \quad (\text{A11})$$

The bandwidth is obtained by considering the range of radii of resonance circles within the loss cone edge, for constant emission angle (corresponding to a fixed centre of the resonance circle). Then, from Equation (A4), the bandwidth is

$$\frac{\Delta \omega}{s \Omega_e} \approx \frac{v_0^2}{2c^2} \Delta \alpha \cos^2 \alpha_{lc} \sin 2\alpha_{lc}. \quad (\text{A12})$$

This expression generalizes the result obtained by Hewitt et al. (1982), for small α_{lc} , to all loss-cone opening angles. The angular width $\Delta \theta$ is estimated from the range of v_0 (centre of resonance circle) within the loss-cone edge, with

$$\Delta \cos \theta = \frac{v_0}{c} \Delta \alpha \cot \alpha_{lc}. \quad (\text{A13})$$

The effect of damping by thermal electrons also needs to be considered. Figure 2 shows a resonance circle which intersects the v_{\parallel} -axis, with $v_{\parallel} = v_0 - V$, at the velocity v_* where the loss-cone distribution merges into the thermal background, with

$$v_* \approx V_{\text{th}} \sqrt{\ln \left(\frac{n_{\text{th}}}{n_{lc}} \right)}, \quad (\text{A14})$$

assuming that $V_{\text{th}} \ll V_{lc}$ and $n_{lc} \leq n_{\text{th}}$. Those resonance circles with

$$v_0 - V \leq v_*, \quad (\text{A15})$$

sample the strong damping region associated with the thermal electrons, and the negative contribution to the integrated growth rate in the thermal region typically far outweighs the positive contribution in the loss-cone region. Hence, from Equations (A3), (A4) and (A14), cyclotron-maser radiation is strongly damped for resonance circle centres less than the critical value

$$v_0 \leq \frac{V_{\text{th}}}{1 - \sin \alpha_{lc}} \sqrt{\ln \left(\frac{n_{\text{th}}}{n_{lc}} \right)}. \quad (\text{A16})$$

In this analysis, we approximate the onset of thermal damping by a step function in Equation (A16).

APPENDIX B: MODE SUPPRESSION

The electron-cyclotron maser can operate in various plasma wave modes; however only waves generated in the magnetoionic x -mode and o -mode can escape to a distant observer. Waves in other modes are trapped in the source region. For maser emission to be generated in the escaping modes, the peak frequency $\omega_{\max,s}$ (Equation A11) must exceed the relevant cutoff frequency, which for the x -mode is (Melrose, 1986, p.171)

$$\omega_x = \frac{1}{2} \Omega_e + \frac{1}{2} (\Omega_e^2 + 4\omega_p^2)^{1/2}, \quad (\text{B1})$$

and for the o -mode is

$$\omega_o = \omega_p. \quad (\text{B2})$$

With increasing plasma density or decreasing magnetic field strength, the ratio ω_p/Ω_e increases such that $\omega_{\max,s}$ lies below the cutoff frequency, and successive harmonics are suppressed. For $\omega_p/\Omega_e \lesssim 0.3$, the condition $\omega_{\max,1} \geq \omega_x$ is satisfied. In this case, growth of the fundamental x -mode saturates the maser, because it has a significantly higher growth rate than other modes (Melrose, Dulk & Hewitt 1984). For higher values of ω_p/Ω_e , fundamental x -mode emission is suppressed, allowing wave growth in the fundamental o -mode and second harmonic x -mode, which have comparable maximum growth rates. The growth rates of higher harmonic x -mode and o -mode waves are too low to produce observable radiation. Trapped modes may also grow (e.g., z -mode, Bernstein modes; Melrose, Dulk & Hewitt 1984; Willes & Robinson 1996); however, these can only escape to an observer after conversion to a free-space mode by linear mode conversion or nonlinear wave-wave processes (Melrose 1991; Willes & Robinson 1996). We only consider growth of free-space modes in this paper. Growth of trapped modes may lower the effective growth rates of the fundamental o -mode and second-harmonic x -mode assumed in this paper if the maser does not saturate (Melrose, Dulk & Hewitt 1984).

Assuming saturation of the maser, only fundamental x -mode emission is generated when the condition $\omega_{\max,1} \geq \omega_x$ is satisfied. Otherwise, fundamental o -mode emission is generated in the parameter range $\omega_o \leq \omega_{\max,1} < \omega_x$, and harmonic x -mode emission is generated for $\omega_{\max,1} < \omega_x \leq \omega_{\max,2}$. Hence there is a wide range of ω_p/Ω_e over which fundamental o -mode and second harmonic x -mode are simultaneously generated. These ranges vary with emission angle θ , through Equations (A7) and (A11). We note that in a more self-consistent treatment of maser emission, where the maser operates in a state close to marginal stability (Robinson 1991), the fundamental o -mode and second-harmonic x -mode compete more effectively with the fundamental x -mode over a wider range of parameters.

APPENDIX C: HARMONIC DAMPING

As maser emission, emitted at $\omega \approx s\Omega_e$, propagates away from the source the local cyclotron frequency decreases with decreasing magnetic field strength, and the radiation approaches a harmonic absorption layer, where $\omega \approx (s+1)\Omega_e$. Absorption at higher harmonic layers ($s+2, s+3, \dots$) may also occur, but the absorption strength falls off rapidly with increasing harmonic number. Assuming a slab geometry, with linearly varying magnetic field strength (scale length $L_B \approx R_1/3$), and constant thermal velocity V_{th} , the optical depth at the s th layer for x -mode radiation satisfies (Kuncic & Robinson 1993)

$$\tau_{\sigma,s}(\omega, \theta) = \frac{\pi L_B \omega}{c} \frac{s^{2s}}{2^s s!} \frac{\omega_p^2}{\omega^2} \left(\frac{V_{\text{th}} \sin \theta}{c} \right)^{2s-2} \times \left[\frac{(1 + T_\sigma \cos \theta)^2 + T_\sigma^2 V_{\text{th}}^2 / c^2}{1 + T_\sigma^2} \right]. \quad (\text{C1})$$